Review

Tin Diselenide (SnSe₂) Van der Waals Semiconductor: Surface Chemical Reactivity, Ambient Stability, Chemical and Optical Sensors

Gianluca D'Olimpio [1], Daniel Farias [2,3,4,*], Chia-Nung Kuo [5,6], Luca Ottaviano [1,7], Chin Shan Lue [5,6], Danil W. Boukhvalov [8,9,*] and Antonio Politano [1,10,*]

1   Department of Physical and Chemical Sciences, University of L'Aquila, via Vetoio, 67100 L'Aquila, Italy; gianluca.dolimpio@univaq.it (G.D.); luca.ottaviano@aquila.infn.it (L.O.)
2   Departamento de Física de la Materia Condensada, Universidad Autónoma de Madrid, 28049 Madrid, Spain
3   Instituto "Nicolás Cabrera", Universidad Autónoma de Madrid, 28049 Madrid, Spain
4   Condensed Matter Physics Center (IFIMAC), 28049 Madrid, Spain
5   Department of Physics, National Cheng Kung University, 1 Ta-Hsueh Road, Tainan 70101, Taiwan; kuochianung@gmail.com (C.-N.K.); cslue@mail.ncku.edu.tw (C.S.L.)
6   Taiwan Consortium of Emergent Crystalline Materials, Ministry of Science and Technology, Taipei 10601, Taiwan
7   CNR-SPIN UoS L'Aquila, Via Vetoio, 67100 L'Aquila, Italy
8   College of Science, Institute of Materials Physics and Chemistry, Nanjing Forestry University, Nanjing 210037, China
9   Theoretical Physics and Applied Mathematics Department, Ural Federal University, Mira Street 19, 620002 Ekaterinburg, Russia
10 CNR-IMM Istituto per la Microelettronica e Microsistemi, VIII strada 5, I-95121 Catania, Italy
*   Correspondence: daniel.farias@uam.es (D.F.); danil@njfu.edu.cn (D.W.B.); antonio.politano@univaq.it (A.P.)

Abstract: Tin diselenide (SnSe₂) is a layered semiconductor with broad application capabilities in the fields of energy storage, photocatalysis, and photodetection. Here, we correlate the physicochemical properties of this van der Waals semiconductor to sensing applications for detecting chemical species (chemosensors) and millimeter waves (terahertz photodetectors) by combining experiments of high-resolution electron energy loss spectroscopy and X-ray photoelectron spectroscopy with density functional theory. The response of the pristine, defective, and oxidized SnSe₂ surface towards H_2, H_2O, H_2S, NH_3, and NO_2 analytes was investigated. Furthermore, the effects of the thickness were assessed for monolayer, bilayer, and bulk samples of SnSe₂. The formation of a sub-nanometric SnO_2 skin over the SnSe₂ surface (self-assembled SnO_2/SnSe₂ heterostructure) corresponds to a strong adsorption of all analytes. The formation of non-covalent bonds between SnO_2 and analytes corresponds to an increase of the magnitude of the transferred charge. The theoretical model nicely fits experimental data on gas response to analytes, validating the SnO_2/SnSe₂ heterostructure as a suitable playground for sensing of noxious gases, with sensitivities of 0.43, 2.13, 0.11, 1.06 [ppm]$^{-1}$ for H_2, H_2S, NH_3, and NO_2, respectively. The corresponding limit of detection is 5 ppm, 10 ppb, 250 ppb, and 400 ppb for H_2, H_2S, NH_3, and NO_2, respectively. Furthermore, SnSe₂-based sensors are also suitable for fast large-area imaging applications at room temperature for millimeter waves in the THz range.

Keywords: van der Waals semiconductors; gas sensing; tin diselenide; density functional theory

1. Introduction

Following the advent of graphene [1–4], the scientific community has begun to consider layered semiconductors for their potential application to complement those of graphene [5–9], thus generating promising new technologies in various technological areas [10–16]. The class of materials of 'van der Waals semiconductors' is characterized by weak van der Waals bonds between the layers that allow their exfoliation by mechanical [17,18] and liquid-phase [19–21] exfoliation.

The most common van der Waals semiconductors have shown limitations, which compromise their technological development. For example, MoS_2 and WS_2 have a poor electric mobility of a few tens of $cm^2V^{-1}s^{-1}$ at T = 300 K [22]; black phosphorus is instable in air and undergoes a rapid surface oxidation which degrades the morphology of the surface [23]; GaSe exhibits instability upon both laser and air exposure [24,25]; and $PdSe_2$ [26,27] has a limited commercial potential, due to the constantly growing price of Pd (2000–2400 \$/oz), nearly doubled in 2019–2021.

Tin diselenide ($SnSe_2$) is a layered semiconductor constituted by Earth-abundant and cheap elements [28], which crystallizes in a layered CdI_2–type structure with hexagonally packed layers of Sn atoms sandwiched between two layers of Se anions (Figure 1a,b) [29–31]. Differently from MoS_2 and WS_2, $SnSe_2$ has a high intrinsic electron mobility at T = 300 K ($462.6\ cm^2V^{-1}s^{-1}$) and ultralow thermal conductivity ($3.82\ W\ m^{-1}\ K^{-1}$) [32]. Furthermore, $SnSe_2$ exhibits pressure-induced periodic lattice distortion and, moreover its atomic structure can reversibly change from amorphous to crystalline upon laser heating, being a phase change memory material. Owing to these peculiarities, $SnSe_2$ has high application capabilities in several fields, including superconductivity [33,34], Li^- [29,35] and Na^- [29,36] ion batteries, photodetection [37], photocatalysis [38,39], saturable absorbers for eye-safe lasers [40], and thermoelectricity [41,42].
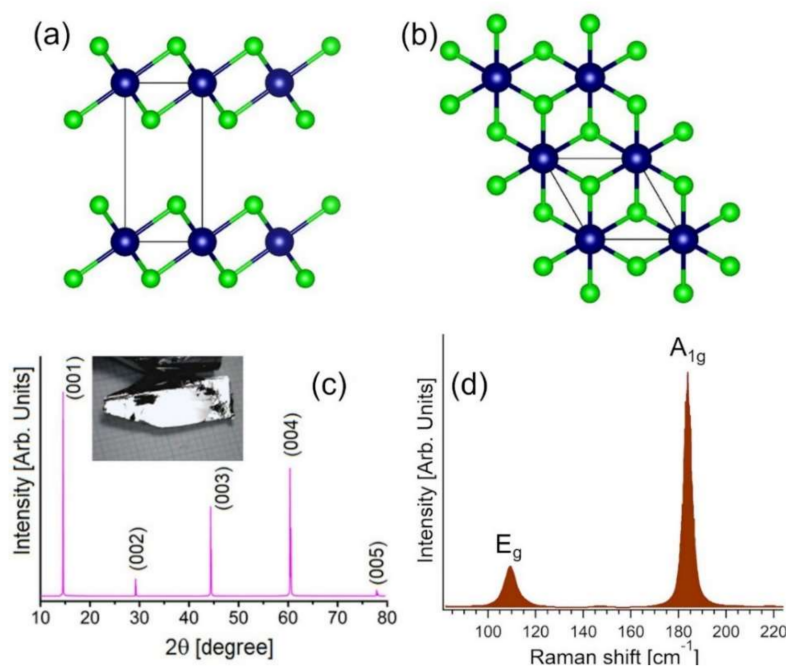
Figure 1. (**a**) Side and (**b**) top views of the atomic structure of $SnSe_2$. Green and blue balls denote Se and Sn atoms, respectively. Panel (**c**) reports the single-crystal XRD pattern from the (001) plane of $SnSe_2$. The inset shows a photograph of an as-grown $SnSe_2$ single crystal. Panel (**d**) reports the Raman spectrum of $SnSe_2$ single crystal acquired at room temperature with a laser with wavelength λ = 632.8 nm.

Nevertheless, Sn-based chalcogenides suffer from rapid surface oxidation with the formation of surface tin-oxide phases [43,44]. Furthermore, during the crystal synthesis process, tin could already oxidize, modifying its overall transport properties [45]. Therefore, the use of Sn-based chalcogenides for technology transfer remains particularly arduous. Especially, stability in ambient atmosphere of $SnSe_2$-based devices is related to the chemical reactivity of its surface.

Here, we unveil surface properties of $SnSe_2$ single crystals by means of surface-science experiments and density functional theory (DFT). We demonstrate that the stoichiometric $SnSe_2$ sample is chemically inert, while the presence of Se vacancies induces surface

oxidation with the formation of a sub-nanometric SnO_2 skin. We also explore the capability of $SnSe_2$ to realize devices for sensors for detecting noxious gases and imaging applications with non-ionizing radiations. Especially, we show that chemical sensing is feasible only when the pristine $SnSe_2$ surface is transformed into an heterostructure of $SnO_2/SnSe_2$. Concerning photodetection, we report the design of broadband $SnSe_2$-based photodetectors interplayed by synergistic effects of multiple mechanisms. Considerably, the effect of hot electrons in ultrashort channel devices under strong light coupling results in outstanding performance in term of high responsivity at THz frequency.

2. Materials and Methods

Single crystals of $SnSe_2$ were grown by Bridgman–Stockbarger (Figure 1c). Stoichiometric ratio of 1:2 was put on evacuated quartz ampoule. The growth was carried out in a vertical two-zone tube furnace. The obtained crystal was characterized with X-ray diffraction (XRD) on powders, as shown Figure 1c. From the XRD spectrum, we can conclude that the crystal structure is CdI_2–type (space group P-3m1). The lattice parameters are a = 0.3804 nm and c = 0.6128 nm consistently with previous works [46–49]. We also carried out the XRD and Laue diffraction measurements on single crystals. Samples were exfoliated in situ by adhesive tape. The absence of contamination in grown single crystals is secured by the survey X-ray photoelectron spectroscopy (XPS) spectrum.

XPS experiments were carried out with synchrotron light at APE-HE beamline at the Elettra Synchrotron in Trieste, Italy.

High resolution electron energy loss spectroscopy (HREELS) experiments were performed with a Delta 0.5 spectrometer (Specs GmbH, Germany). Spectra were taken in specular geometry, with an impinging angle of 55° with respect to the perpendicular direction to the surface. The impinging energy is 3.5 eV.

Theoretical methods are reported in Section S1 of the Supplementary Materials.

Fabrication process and measurements of devices are reported in section S2 of the Supplementary Materials.

3. Results

3.1. Chemisorption of O_2 and H_2O on Bulk $SnSe_2$

The Raman spectrum of the grown $SnSe_2$ single crystal (Figure 1d) shows the E_g and A_{1g} modes at 109 and 184 cm^{-1}, respectively, congruently with previous reports [50–52]. The narrow (00l) diffraction peaks (Figure 1c) reveal the excellent crystallinity for our $SnSe_2$ crystals.

To model surface chemical reactivity, the differential enthalpy ΔH_{ads} and the differential Gibbs free energy ΔG for the adsorption of water and oxygen at room temperature, as well as the decomposition energy ΔH_{dec} for both gases were calculated. The possibility of different kinds of defects was energetically evaluated and the formation of one Se vacancy is particularly feasible (only 1.28 eV/Se). The influence of Se vacancies was explored from a single vacancy in the outermost surface layer (Figure 2a) up to larger concentration of Se vacancies. We also calculated the different possible positions for a second Se vacancy, finding that the most energetically favorable location (0.98 eV/Se) is to have the second vacancy in the next neighbor to the first vacancy. To model such a large number of vacancies, an outermost SnSe-like layer on the surface was also considered (Figure 2b). Calculations indicate that physisorption of molecular oxygen is feasible at all investigated surfaces, although it is more energetically favorable at Se vacancies ($\Delta G = -26.3$ kJ/mol) rather than on defects-free $SnSe_2$ ($\Delta G = -3.2$ kJ/mol). The subsequent decomposition of molecular oxygen is an exothermic process for $SnSe_2$, $SnSe_{1.88}$, and SnSe. However, in the case of $SnSe_{1.88}$ and SnSe the differential enthalpy of decomposition is much lower than the defect-free $SnSe_2$ (-135.7, -236.1, and -42.3 kJ/mol, respectively). Thus, the oxidation rate should be greater on defective surfaces of $SnSe_2$. After the decomposition of a single oxygen molecule, we assess the oxygenation of the whole surface, corresponding to an atomic structure with oxygen atom attached to each surface Se atom, and the successive

oxidation in a metastable surface $SnSe_2O_2$ phase (see Figure 2c), whose lifetime is estimated to be < 1 ms and, consequently, its presence on the surface could be detected only with time-resolved experiments. Hence, first the Se atoms in the $SnSe_2O_2$ migrate to occupy the Se vacancies formed in the subsurface region and then the oxygen atoms from the $SnSe_2O_2$ oxidize the Sn atoms of the surface layer to form SnO_2, see Figure 2d. The following chemical equation can describe this process as

$$O_2 + SnSe_2 + SnSe_{2-y} \rightarrow SnSe_2O_2 + SnSe_{2-y} \rightarrow SnO_2 + 2Se + SnSe_{2-y} \rightarrow SnO_2 + SnSe_{2-x} \tag{1}$$
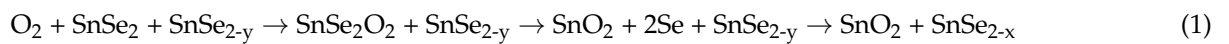
with x < y, where $SnSe_{2-y}$ corresponds to Se defects in the substrate, which are partially or totally saturated by Se freed from top layer after formation of SnO_2-skin.
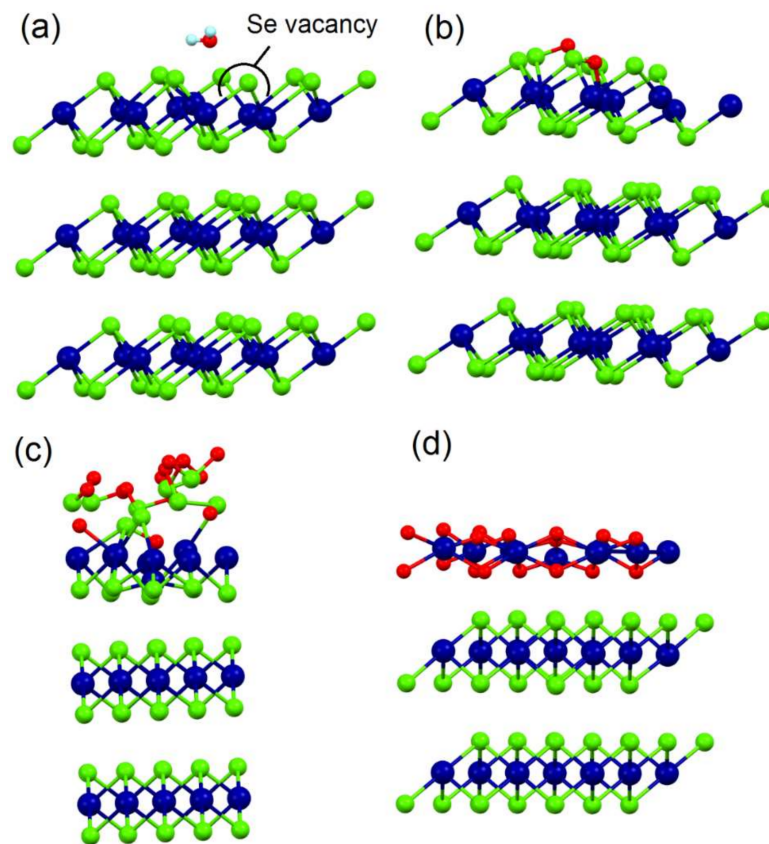

Figure 2. Optimized atomic structure of (**a**) water molecules physisorbed at one Se-vacancy site; (**b**) decomposed oxygen molecule on SnSe surface layer; (**c**) metastable $SnSe_2O_2$ surface layer; and (**d**) SnO_2-skin-terminated $SnSe_2$.

We calculated the necessary energy to heal the Se vacancy by extracting Se from the SnO_2 skin and the differential enthalpy for this reaction is −3.54 eV/Se for the oxidized surface of $SnSe_2$ and −2.97 eV/Se for oxidized surface of $SnSe_{1.88}$. These values cause a preferential oxidation of Sn with respect to Se and, subsequently, the surface oxide layer should be modelled as a $SnO_2/SnSe_2$ heterostructure.

Instead, the physisorption of water is energetically unfavorable on $SnSe_2$. Although near the Se vacancy the energy barrier for water absorption decreases it always remains a metastable process with positive ΔG in the Se vacancy sites (ΔG = +3.4 kJ/mol). Even in the defect sites, a subsequent decomposition of water is extremely unfavorable (ΔH_{dec} = +175.7 kJ/mol). This behavior can be understood because the water molecules interact with diselenides via the formation of non-covalent bonds between lone pairs of electrons on *sp* orbitals of oxygen and unoccupied orbitals of metal centers in substrate. In

the case of SnSe$_2$, some mismatch between the size of water molecule and lattice parameters of the substrate is not so favorable for the formation of the described non-covalent bonds. The contribution to the adsorption energy calculated from the energy cost of the substrate and molecule distortions decreases ΔH, making it lower than the TΔS contribution in the ΔG calculation. In the case of adsorption on an oxidized substrate, hydrogen bonds are established between water and substrate oxygen. The formation of these hydrogen bonds can occur at much broader range of positions of water on the substrate and, therefore, no contribution in ΔH comes from distortions of either substrate or water.

3.2. Experimental Validation of the Theoretical Model

Probing vibrational modes could afford additional information on surface chemical processes and, especially, physicochemical mechanisms ruling the formation of an oxide skin. In particular, high-resolution electron energy loss spectroscopy (HREELS) experiments on H$_2$O-exposed tin selenides SnSex, with x ranging between 1 and 2 (SnSe, SnSe$_{1.4}$, SnSe$_{1.7}$, SnSe$_2$), indicate the lack of chemisorbed molecules resulting from the presence of H$_2$O, this is evident from the absence of O-H streching at 410–420 meV (molecular water) and 450 meV (hydroxyl groups) in the spectra in Figure 3 [53]. These findings are consistent with the positive Gibbs free energy of adsorption (corresponding to energetically unfavorable water adsorption) in Table 1. For a better comparison, we report in Figure 3 the vibrational data obtained by exposing other chalcogenides to the same dose of water (10^5 L). Unlike the surface of SnSex, a stable adsorption of water molecules was found on PtTe$_{1.6}$ and, moreover, of hydroxyl groups on InSe. The absence of reactivity toward water of Sn-based chalcogenides makes them suitable for catalysis (in particular, photocatalytic water splitting [38], and hydrogen evolution reaction [54]) and drug delivery [55] (also bearing in mind that neither Sn nor Se are toxic).
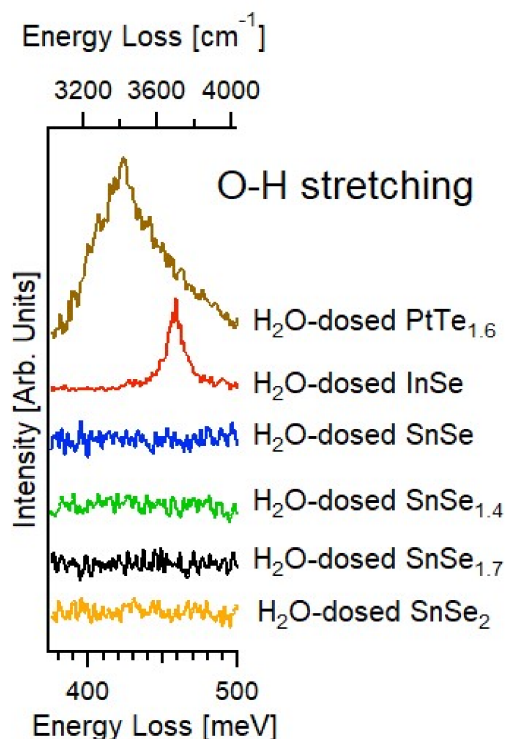
**Figure 3.** Vibrational spectra around the energy of O-H intramolecular stretching, recorded upon dosing to 10^5 L of H$_2$O at T = 300 K the surfaces of various tin-based selenides: SnSe$_2$ (orange), SnSe$_{1.7}$ (black), SnSe$_{1.4}$ (green), and SnSe (blue). We also report vibrational acquired in the same conditions for water-dosed InSe (red) and PtTe$_{1.6}$ (brown). The energy of the primary electron beam is 4 eV.

Table 1. Differential enthalpy ΔHads and differential Gibbs free energy ΔG for physisorption at room temperature and differential enthalpy of decomposition ΔH_{dec} for molecular oxygen and water on the surface of bulk samples of $SnSe_2$, $SnSe_{1.88}$, and SnSe. For the decomposition of oxygen, we also report, in parenthesis, the differential enthalpy for the formation of an oxygenated surface and a SnO_2-like layer.

Surface	Adsorbant	Physisorption		Decomposition
		ΔH_{ads} (kJ/mol)	ΔG (kJ/mol)	ΔH_{dec} (kJ/mol)
$SnSe_2$	O_2	−17.5	−3.2	−42.3 (−161.6/~ −40.2)
	H_2O	−13.3	+18.0	+220.9
$SnSe_{1.88}$	O_2	−37.6	−26.3	−135.7 (−99.1/−406.7)
	H_2O	−27.9	+3.4	+175.6
SnSe	O_2	−11.6	−0.2	−236.1 (−323.1/+95.4)
	H_2O	−8.1	+23.2	+82.2
SnO_2 skin	H_2O	−119.7	−106.7	−121.3

Notably, the vibrational spectrum of the oxidized $SnSe_2$ surface (Figure 4a) closely overlaps with the phonon excitation spectrum of SnO_2 [56]. Definitely, modes at 48, 99, 126, 177, and 219 meV were measured. In particular, the loss peaks at 48 (A_{2g} phonon) and 99 (B_{2g} phonon) meV are blue-shifted by 4 and 10 meV in the disordered tin-oxide skin formed upon oxidation of $SnSe_2$ compared to their respective value for bulk SnO_2 crystals [56].
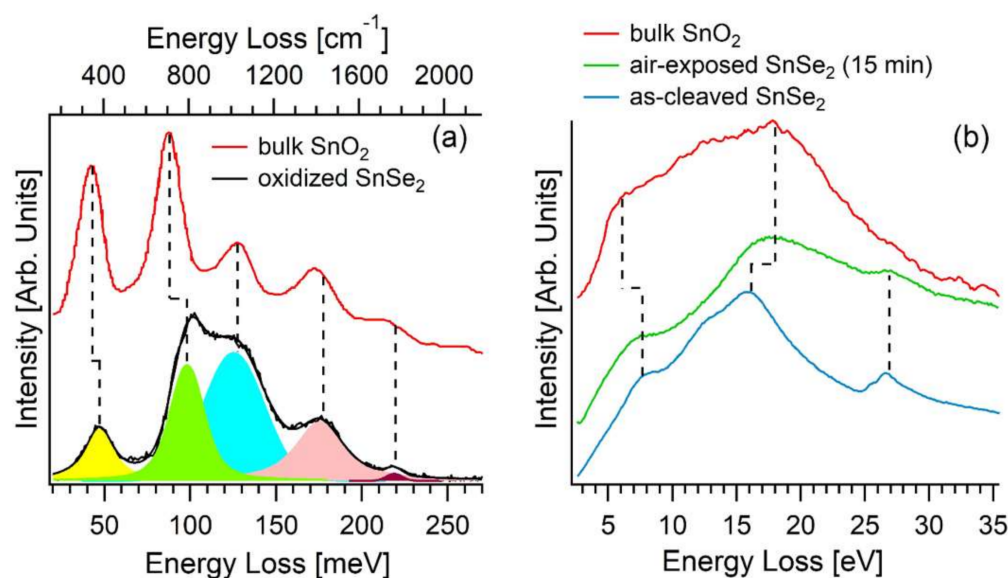
Figure 4. (**a**) Vibrational data for oxidized $SnSe_2$(001) (recorded by HREELS with impinging energy of 4 eV) and bulk SnO_2(110) (data taken from [56]). (**b**) Excitation spectrum for pristine and air-modified $SnSe_2$ (recorded by EELS with impinging energy of 300 eV) and bulk SnO_2 (data taken from [57]).

The inspection of the excitation spectrum probed by EELS, extended up to the ultraviolet range of the electromagnetic spectrum (Figure 4b), enables monitoring the surface status with a technique with probing depth as low as (0.9 ± 0.1) nm in our experimental conditions [58], which is lower by more than 10^2 with respect to Raman spectroscopy and optical techniques. Specifically, the excitation spectrum of the as-cleaved $SnSe_2$ surface shows a main feature at 15.9 eV with a shoulder at 12.0 eV, ascribed to interband transitions from Se-4s core levels and, moreover, two weak losses at 7.5 and 26.8 eV. The excitation spectrum of the air-exposed $SnSe_2$ sample is dominated by an emerging broad

mode centered around ~18 eV, with two weak peaks at 7.5 and 26.8 eV, evidently insensitive to surface modification. Notably, polycrystalline SnO_2 films display the feature at 18.0 eV. Precisely, this feature was previously attributed to the sub-oxide SnO_{2-x} phases [59]. However, the inspection of density of states (DOS) in Figure 5 reveals that the mode at 18.0 eV is related to a single-particle transition starting from O-2s band in SnO_2. The weak peaks at 7.5 and 26.8 eV are ascribed to interband transitions originated by Sn-5*s* and Se-3*s* levels, respectively.
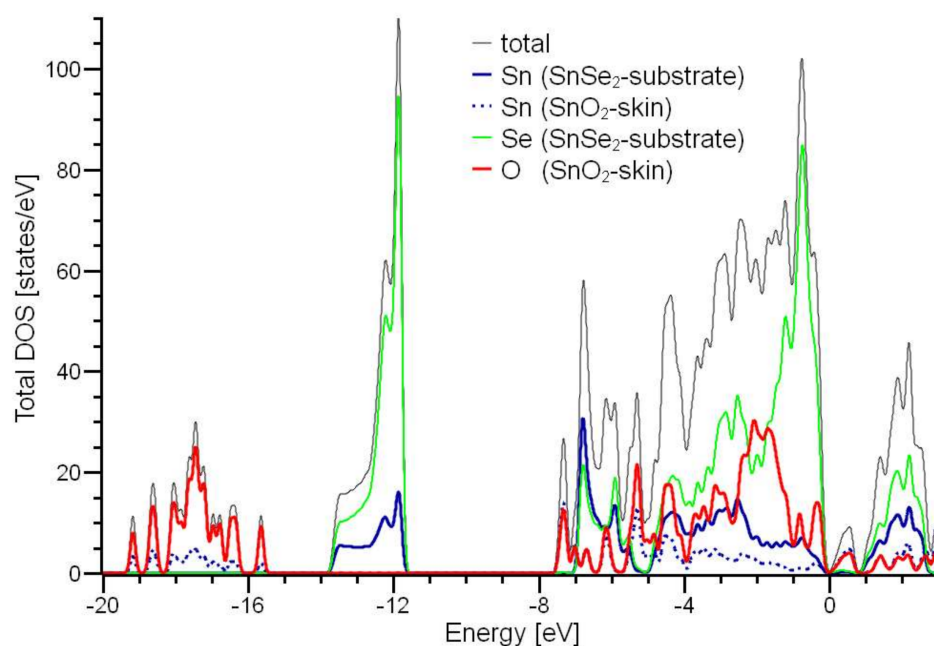

Figure 5. Partial densities of states for $SnSe_2$ slab with SnO_2-skin (see Figure 2d). Fermi energy is set as zero.

Further information on the surface properties was provided by the inspection of core levels by means XPS experiments performed on both pristine and powderized $SnSe_2$ single crystals. As a matter of fact, it is also important to assess the characteristics of the powderized material with the future implementation in devices in mind, for which the surface/volume ratio should be maximized in order to improve the performance. Figure 6 shows the Sn-3d and Se-3d core levels of the as-cleaved $SnSe_2$ single-crystal surface and for the same surface modified by O_2 dosage with a total dose of 10^5 L (1 L = 10^{-6} Torr·s). The Sn-$3d_{5/2}$ core level of the as-cleaved sample has a binding energy (BE) of 486.8 eV (Figure 6a). Correspondingly, the Se-3d core levels exhibit a single peak with the J = 5/2 component located at BE = 54.1 eV, compatibly with previous reports for $SnSe_2$ [60] and with a lower BE compared to the case of SnSe (BE = 53.7 eV). Exposure to 10^5 L of oxygen and storage in air only caused a slight change in the core level of the Se-3d. A new component at BE = 54.7 eV in Se-3d core level arising from Se(0) segregation is observed [61]. The total spectral area of this new component is 5.4% for O_2 dosage and 2.6% for air exposure. Especially, from the Se-3d core-level spectra (Figure 6b) one can observe the absence of the SnO_2 component, which would be characterized by the J = 5/2 component at BE of ~59–60 eV.
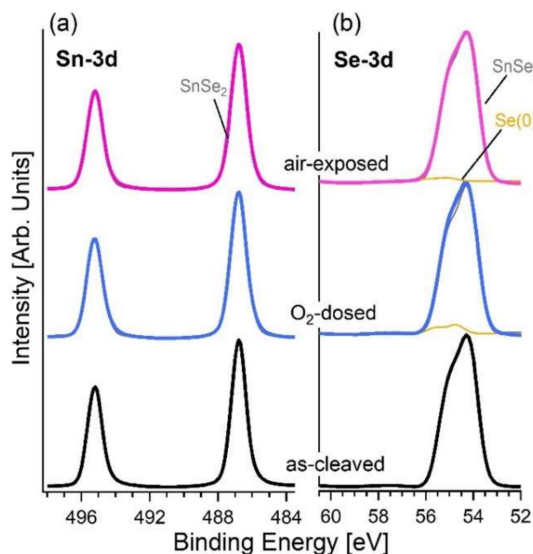
Figure 6. Panels (**a**) and (**b**) show Sn-3d and Se-3d core levels for as-cleaved surface of $SnSe_2$ and its modification upon O_2 (10^5 L) dosage and air exposure. The photon energy is 800 eV.

Conversely, in the powderized single crystal, one spectral component arising from surface oxidation was found (Figure 7). Specifically, the new component in the $Sn-3d_{5/2}$ core level related to SnO_2 was observed at BE = 487.8 eV (54% of the total spectral area) [62,63]. Remarkably, even after powderization, no trace of SeO_2 is present, as indicated by the featureless Se-3d spectra in the range 59–60 eV [64]. This finding confirms our prediction that Se is only involved in a metastable oxide phase, which represents a precursor for SnO_2 formation. However, in the powderized sample, a different Se oxidation state is present, as revealed by a broad feature in the spectra. Precisely, we assign the component at 55.0 eV to Se^{-2} and the higher to $Se^{-2+\delta}$ ($0 < \delta < 1$) [65]. In the powderized sample, we estimate δ to be ~0.15 $\pm$ 0.05 from the analysis of the survey XPS spectrum. Therefore, sub-stoichiometric $SnSe_{1.7\pm0.1}$ coexists with $SnSe_2$. We also estimated the thickness of the SnO_2 surface layer by means of quantitative analysis of XPS data [66], finding a thickness of (0.8 $\pm$ 0.1) nm (~2.5 monolayers) without observable changes after an exposure of one week in air. It should be noted that previous reports indicated that the surface of sub-stoichiometric $SnSe_2$ ($SnSe_{1.71}$) grown by molecular beam epitaxy [67] is unstable, with the subsequent formation of SnO_x and SeO_x phases. Conversely, in our case, both SnO and SeO_x are not present on the surface.
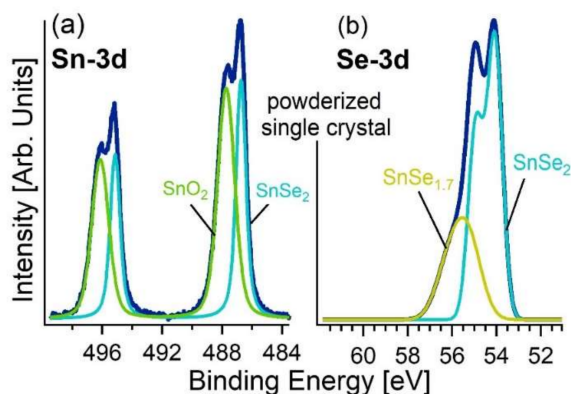

Figure 7. (**a**) Sn-3d and (**b**) Se-3d core levels of powderized $SnSe_2$ single crystal. Note that grinding of $SnSe_2$ bulk crystals was carried out in ambient atmosphere. The photon energy is 1486.6 eV (Al K_α).

The $SnO_2/SnSe_2$ heterostructure is more sensitive to chemisorbed species with respect to pristine $SnSe_2$. On the pristine surface, the absorption of water molecules generates local changes in charge density in proximity to the absorbed molecules on the surface layer due to a rearrangement of chemical bonds, with a charge transfer of 0.17 e- per water molecule (Figure 8a). Thus, we conclude that pristine $SnSe_2$ is unsuitable for humidity sensing. On the other hand, the absorption of H_2O on $SnO_2/SnSe_2$ is energetically favorable even above room temperature. We calculated the values of transferred charge from H_2O to the SnO_2 skin that are 0.43 and 0.30 e^- for one and two H_2O molecules per supercell, respectively. Correspondingly, the density of states (DOS) is modified with a direct correlation with the coverage of the adsorbate (Figure 8b–d), thus indicating the suitability for humidity sensing, even at the lowest concentrations of H_2O. Note that decomposition of water molecule on the $SnO_2/SnSe_2$ heterostructure is an exothermic process (-121.4 kJ/mol) and the subsequent water splitting is unfavorable, favoring the reversibility of the process. This further supports the use of the self-assembled $SnO_2/SnSe_2$ heterostructure for humidity sensing.
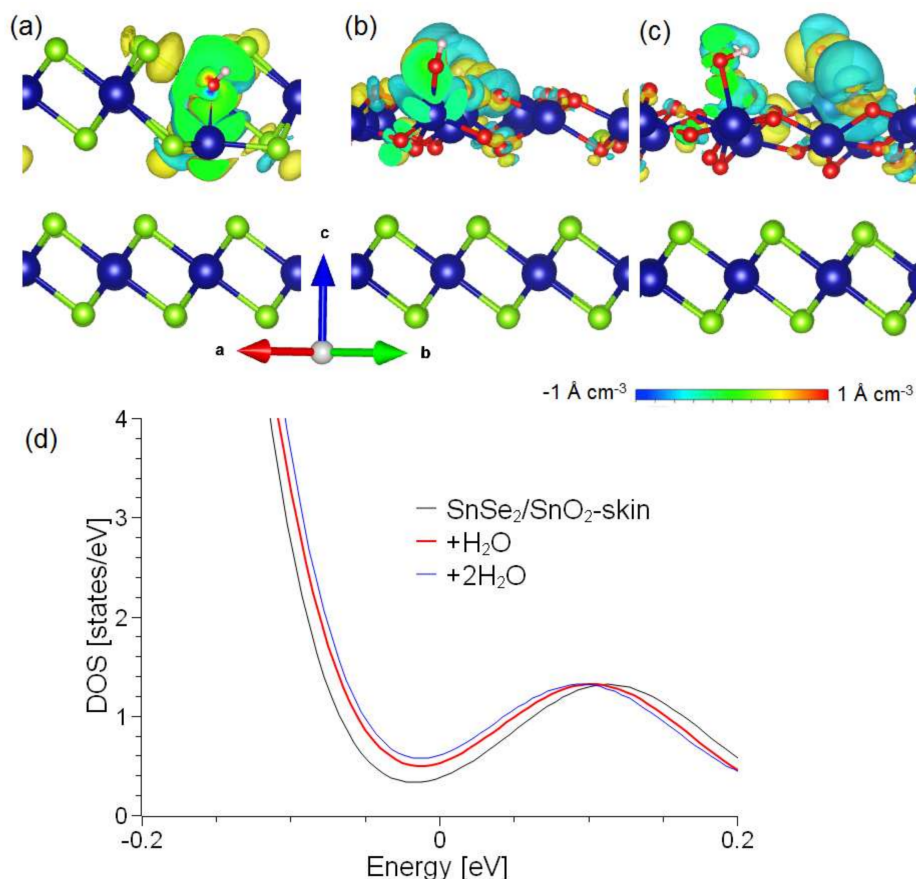
Figure 8. Panels (**a-c**) report the change of the charge density after adsorption of one water molecule on $SnSe_2$, one water molecule on SnO_2-skin-terminated $SnSe_2$, and two water molecules on SnO_2-skin-terminated $SnSe_2$, respectively. Panel (**d**) represents the DOS of SnO_2-skin-terminated $SnSe_2$ (black curve) and of the same system modified by the adsorption of one (red curve) and two (blue curve) water molecules. Fermi level is set at 0.

3.3. Gas Sensing

The evaluation of the stability of $SnSe_2$-based systems at the temperature of 200 °C, used in a typical gas sensing experiment, was performed. For the surface model of bulk $SnSe_2$, trilayers of $SnSe_2$ with fixed lattice parameters were used. For free-standing bi- and monolayer optimization of both atomic position and lattice parameters was performed. This provides the contribution in the energetics of the adsorption from flexibility of free-

standing few-layers. In order to make calculations more realistic, we also considered the presence of the Se vacancies in the top layer. The formation of the single vacancy turns the $SnSe_2$ to $SnSe_{1.88}$. Results of the calculations (see Table 2) demonstrate that physical adsorption on bulk and few-layers of $SnSe_2$ is unfavorable at 200 °C. Contrarily, the presence of Se-vacancies makes physisorption favorable. The decomposition of molecular oxygen is favorable in all cases except for monolayer $SnSe_{1.88}$. This exception is due to the combination of distortions caused by the presence of vacancies and distortions created by formation of new Se-O chemical bonds. Note that this result is valid only for free-standing monolayers. In fact, the deposition of a free-standing monolayer on a substrate decreases the flexibility of $SnSe_x$ and makes the system closer to a $SnSe_x$ bilayer.

Table 2. Differential enthalpy (ΔH_{phys}) and Gibbs free energy (ΔG) at an operational temperature of 200 °C for the physisorption of molecular oxygen at the surface of bulk, bilayer, and monolayer $SnSe_2$ and $SnSe_{1.88}$. The differential enthalphy for oxygen decomposition (ΔH_{dec}) is also reported. All energies are expressed in kJ/mol.

System	Surface	ΔH_{phys} (kJ/mol)	ΔG_{phys} (kJ/mol)	ΔH_{dec} (kJ/mol)
Bulk	$SnSe_2$	−17.5	+5.24	−42.3
	$SnSe_{1.88}$	−37.6	−14.88	−135.7
Bilayer	$SnSe_2$	+38.9	+61.6	−76.3
	$SnSe_{1.88}$	−47.6	−24.9	−115.5
Monolayer	$SnSe_2$	+53.1	+75.8	−56.3
	$SnSe_{1.88}$	−59.3	−36.6	+183.5

The favorability of decomposition of oxygen molecule even at defects-free substrate of $SnSe_2$ could be a starting point for a possible oxidation in the defective areas of $SnSe_2$ (vacancies, edges, grain boundaries). The formation of SnO_2 skin on the surface of bulk $SnSe_2$ leads to a migration of Se-atoms to subsurface area with the passivation of Se-vacancies in the sub-surface layers [68]. In the case of free-standing few layers of $SnSe_x$, an unstable structure would be formed. Therefore, we exclude this configuration from further investigation. Precisely, the discussed unstable structure is related to few free-standing layers, but if we include the presence of the substrate, the formation of more ordered SnO_2 skin will occur. Thus, results obtained for $SnSe_2/SnO_2$ could be extended to few layers of $SnSe_2$ deposited on a substrate.

Considering the possibility of the oxidation with the formation of a SnO_2 skin, we modeled the physisorption of different analytes on $SnSe_x$ and on the SnO_2 skin over $SnSe_2$ substrate (Figure 9). Results of the calculations (see Table 3) demonstrate that the adsorption of various molecules on $SnSe_x$ surfaces obeys the same principles as in the case of oxygen. Definitely, defect-free $SnSe_2$ surface is nearly inert for all considered analytes. The presence of Se vacancies turns the free energy in a negative value making the adsorption favorable. Similarly, the adsorption of all analytes on monolayer $SnSe_x$ is less favorable than the case of bilayer and bulk. In contrast to non-oxidized $SnSe_x$ substrates, the formation of SnO_2-skin corresponds to a strong adsorption of all analytes. The formation of non-covalent bonds between SnO_2-substrate and analytes corresponds to an increase of magnitude of the transferred charge (see Figure 8). Note that the magnitudes of the free energies of adsorption and transferred charges in the case of SnO_2 skin are much larger than in the case of adsorption on Se-vacancies ($SnSe_{1.88}$ surfaces). Additionally, in the case of the adsorption on the SnO_2 skin, the value of the transferred charge is strongly distinct for different analytes.
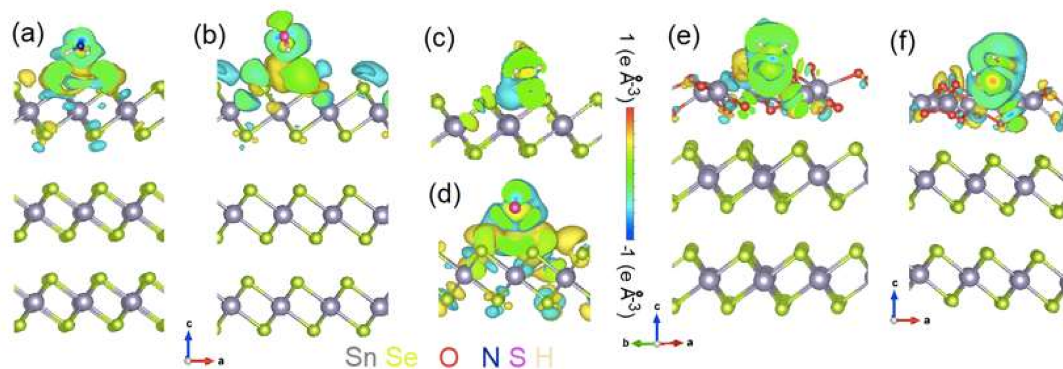
Figure 9. Change of charge densities after adsorption of (**a**,**c**,**e**) NH_3 and (**b**,**d**,**f**) H_2S on (**a**,**b**) bulk and (**c**,**d**) monolayer of $SnSe_2$ and, moreover, (**e**,**f**) the SnO_2 skin on an underlying $SnSe_2$ substrate.

Table 3. Differential Gibbs free energies ΔG of physisorption at 200 $^\circ$C and corresponding values of transferred charge for various combination of considered substrates and analytes

Substrate	Analyte	ΔG (kJ/mol)	Δe^-
Bulk $SnSe_2$ ($SnSe_{1.88}$)	H_2	+6.79 (−0.11)	+0.09 (+0.10)
	H_2O	+45.63 (−30.97)	−0.17 (−0.20)
	H_2S	+38.70 (−21.32)	−0.12 (−0.14)
	NH_3	+24.50 (−12.10)	+0.06 (+0.12)
	NO_2	+58.87 (−36.75)	−0.07 (−0.10)
Bilayer $SnSe_2$ ($SnSe_{1.88}$)	H_2	+8.91 (−0.10)	+0.08 (+0.10)
	H_2O	+41.23 (−26.8)	−0.15 (−0.18)
	H_2S	+36.14 (−29.65)	−0.10 (−0.13)
	NH_3	+18.91 (−10.01)	+0.10 (+0.15)
	NO_2	+46.75 (−25.44)	−0.10 (−0.11)
Monolayer $SnSe_2$ ($SnSe_{1.88}$)	H_2	+2.89 (−4.63)	+0.10 (+0.09)
	H_2O	+28.97 (−7.11)	−0.15 (−0.20)
	H_2S	+18.35 (−0.12)	−0.12 (−0.09)
	NH_3	−4.91 (−12.10)	+0.16 (+0.15)
	NO_2	+0.12 (−3.45)	−0.09 (−0.10)
SnO_2/$SnSe_2$	H_2	−135.61	+0.15
	H_2O	−60.80	−0.43
	H_2S	−71.28	−0.36
	NH_3	−96.20	+0.44
	NO_2	−127.35	−0.25

The theoretical model discussed above was confirmed by experiments. The sensing properties of SnO_2/$SnSe_2$ heterostructures were measured by monitoring the resistance change upon exposure to different concentrations of gases. In Figure 10, the dynamic response-recovery curve with NH_3 (40 ppm) and NO_2 (1 ppm) is shown, with opposite signs in the response curve related to the opposite charge transfer, as depicted in the inset. Interestingly, sub-ppm limit of detection is feasible for both cases, with 250 and 400 ppb for NH_3 and NO_2, with near-room-temperature operational temperatures.

The SnO_2/$SnSe_2$ heterostructure exhibit significantly enhanced response and superb response/recovery characteristics, also for H_2S, for which the lowest detection limit reaches 10 ppb with a response value of 2, which is below the acceptable ambient levels of 20–100 ppb set by the Scientific Advisory Board on Toxic Air Pollutants (USA) [69,70].

Similarly, H_2 detection is feasible using SnO_2/$SnSe_2$ heterostructure [68] with a response of 3 with an operational temperature of 150 $^\circ$C at a concentration of 100 ppm and a limit of detection of 5 ppm. Considering the quite reduced costs of raw elements, this

could be relevant considering that in the growing market for H_2-powered devices—i.e., fuel cells—there is a requirement for cheap H_2 sensors.

Table 4 reports an overview of literature results on near-room-temperature sensing of H_2, H_2S, NH_3, and NO_2 for $SnSe_2$- and SnO_2-based sensors, at their respective operational temperature and concentration. Sensitivities of 0.43, 2.13, 0.11, and 1.06 $[ppm]^{-1}$ were reported for H_2, H_2S, NH_3, and NO_2, respectively (Table 5, also reporting the limit of detection).

The $SnO_2/SnSe_2$ heterostructure exhibits higher performance in terms of high response to analytes, low detection limit, high selectivity, and low power consumption [69–74]. Therefore, based on both calculations and experiments, one can conclude that the $SnO_2/SnSe_2$ heterostructure is a promising platform for gas sensing.

Table 4. Sensing of H_2, H_2S, NH_3, and NO_2 for $SnSe_2$- and SnO_2-based systems. The response obtained at the respective operational temperature and gas concentration is reported. RT means room temperature.

Gas	Sensing Materials	Operational Temperature (°C)	Concentration (ppm)	Response	Reference
H_2	$SnO_2/SnSe_{2-x}$	150	100	3	[68]
H_2	SnO_2	150	1000	5.5	[75]
H_2S	SnO_2	100	10	1–6	[76]
H_2S	$SnSe_2$	RT	10	10–15	[77]
H_2S	$SnO_2/SnSe_2$	RT	10	32	[70]
H_2S	SnO_2	RT	50	33	[78]
NH_3	$SnO_2/SnSe_2$	RT	100	2	[70]
NH_3	$SnSe_2$	RT	40	2.7	[79]
NH_3	$Au-SnSe_2$	RT	5	5.3	[80]
NO_2	$SnO_2/SnSe_2$	RT	10	3.5	[70]
NO_2	$SnO_2/SnSe_{2-x}$	150	1	3.2	[68]
NO_2	$SnSe_2$	RT	1	6	[79]
NO_2	$SnSe_2$	RT	5	112	[81]
NO_2	$SnSe_2/SnSe$	RT	1	75	[82]
NO_2	$Au/SnSe_2$	130	8	3	[83]
NO_2	$Pt-SnSe_2$	130	8	3.9	[83]
NO_2	$SnSe/SnSe_2$	RT	5	12	[84]
NO_2	$SnSe_2$	RT	8	1.4	[85]
NO_2	SnO_2	100	10	1	[76]

Table 5. Sensitivity to H_2, H_2S, NH_3, and NO_2 for $SnSe_2$-based sensors, as well as their limit of detection.

| Gas	Sensitivity $[ppm]^{-1}$	Limit of Detection
H_2	0.43 ± 0.02 [68]	5 ppm at 150 °C [68]
H_2S	2.13 ± 0.01 [77]	10 ppb at RT [70]
NH_3	0.11 ± 0.01 [80]	250 ppb at RT [80]
NO_2	1.06 ± 0.03 [68]	400 ppb at 150 °C [68]
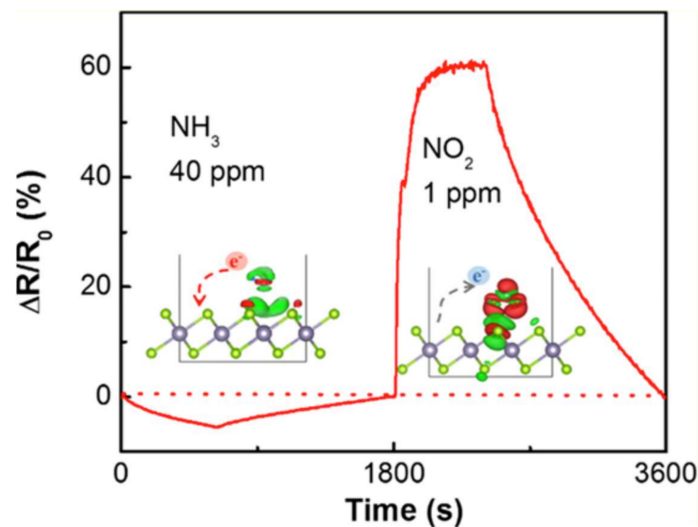
Figure 10. Dynamic response-recovery curve for NO_2 (1 ppm) and NH_3 (40 ppm). The inset depicts that electronic charge transfer occurs from $SnSe_2$ to NO_2, while the opposite charge transfer exists in the case of NH_3, congruently with experimental findings on electrical tests. Reproduced with permission from [79].

3.4. $SnSe_2$-Based Sensors for Large-Area Imaging with Millimetre Waves

An efficient THz detector at room temperature needs two characteristics: high mobility and a channel with nanometer length in a FET. Alternatively, the electron heat-driven detection mechanism could be used [86], based on the specific geometry of the device and the thermal/electrical properties of the material. In fact, $SnSe_2$ has both a high thermoelectric power and a suitable bandgap [87], which are advantageous characteristics for the production of hot electrons and for photothermal conversion. To improve the THz photodetection performance of the $SnSe_2$-based device, the relationship between channel length and photoresponse should be investigated. In FETs, an important issue concerning THz detection is that the channel length should be less than tens of nanometers at the expense of rectification ratio. As mentioned above, it is possible to exploit hot electrons to overcome this limit, related to the absorption efficiency of photons. Specifically, the performance of $SnSe_2$-based THz detectors with a channel length of 6 µm and 100 nm, along with the simulated electric field intensity, were evaluated (Figure 11a). A short channel $SnSe_2$ device is reported in Figure 11a-i,ii. In Figure 11a-iii, one can notice how the reduction of the antenna gap increases the value of the square of the electric field intensity (E_0^2) in the channel by almost three orders of magnitude. To study the different photoelectric properties of the devices as a function of the channel length, the photocurrent, the response time, and the reactivity were measured simultaneously using two radiations 0.04 and 0.12 THz with a power density of 2.5 and 1 mW cm^{-2}, respectively. The photocurrent increases linearly under electrical bias as V_{DS} from −0.1 to 0.1 (Figure 11b), due to the increased carrier drift-velocity and reduced carrier transit time. Moreover, the short channel devices show a photocurrent greater than three orders of magnitude at 0.04 THz, congruently with the theoretical predictions of Figure 11a-iii. By exploiting the antenna gap in short channel device, it is possible to concentrate the THz radiation in a very small spot, consequently improving the $SnSe_2$ intraband absorption capacity, thus hot carriers can be efficiently produced [88]. In Figure 11c, one can observe a good linearity over a wide range of the photocurrent, of the short channel device, as a function of the incident power. Using the equation $I_{ph} \propto P^\beta$ to fit the experimental data, β is ~0.98 under positive or negative bias, which is an interesting value for high-contrast imaging. Even at the frequency of 0.12 THz, there is the same improvement effect, as evident from Figure 11d, confirming the broadband nature of THz field nano-focusing. Additionally, the response time at 0.12 THz

for both short and long channel devices was also studied (Figure 11e). For the short channel device, τ_{rise} = 2.7μs and τ_{fall} = 2.3 μs—i.e., a response time of approximately 16 times faster than in the long channel device (τ_{rise} = 45.4 μs, τ_{fall} = 46.5 μs). Obviously, the long channel device has a slower response time than the short channel device, making the short channel device advantageous in applications. The increase in V_{DS} rapidly increases the bias voltage response to 0.12 THz (Figure 11f). For short channel devices, the maximum response is 2.5 A W^{-1}, which is approximately five times larger than graphene-based devices (20 V W^{-1}) [89] and 12 times larger than black-phosphorus-based devices (7.8 V W^{-1}) [90]. This indicates that short-channel SnSe$_2$ devices have superior performance respect to graphene- and black phosphorus-based devices.
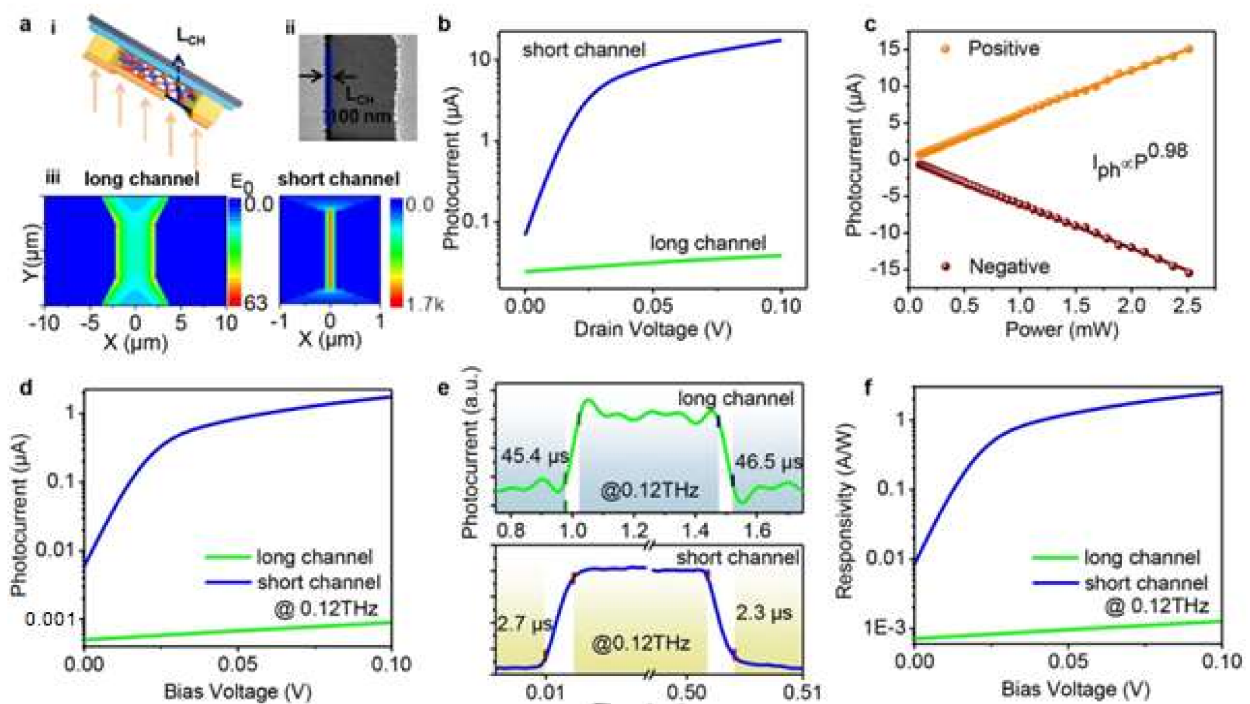

Figure 11. (**a**i) Schematization of the realization of the short-channel device. (**a**ii) Image of a short channel SnSe$_2$-based photodetector acquired with the SEM. (**a**iii) The electric field distribution of the SnSe$_2$-based long channel (left panel) and short channel (right panel) photodetector. (**b**) and (**c**) Photocurrent as a function of the bias voltage and incident power at 0.04 THz, respectively. (**d**) Photocurrent as a function of bias voltage at 0.12 THz. (**e**) (top panel) Long channel and (bottom panel) short channel time-resolved photocurrent devices at 0.12 THz with 1 mW cm^{-2} power. (**f**) Photoresponsivity vs. bias voltage at 0.12 THz with 1 mW cm^{-2} power. Reproduced with permission from [91].

Exploiting the excellent performance of the SnSe$_2$, a large area imaging device with THz transmission was created for identifying hidden objects. Using a radiation of 0.12 THz, the shape of the glue-jar in the box was clearly visible (see Figure 12b). Furthermore, it was possible to detect not only the shape of the glue-jar but also the position of the amount of the glue inside the jar. Another key feature of the THz detector is its stability. Differently from black phosphorus [92], SnSe$_2$-based devices exhibited better stability, congruently with the ambient stability assessed in Figure 6 by surface-science techniques. The absence of noticeable modifications in the photocurrent at 0.12 THz radiation after a prolonged storage in air (extended up to one month, Figure 12a) corroborates the excellent stability of SnSe$_2$-based optoelectronic devices.
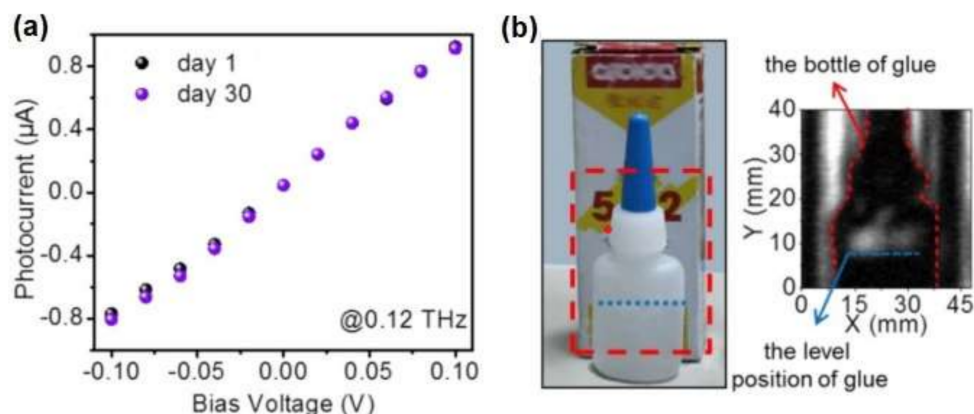
Figure 12. (**a**) Aging in air of SnSe$_2$-based short channel photodetector, black and purple spot represent the photocurrent of as-prepared device and after 30 days in air, respectively. (**b**) The THz imaging of a glue-jar in the box at 0.12 THz. Reproduced with permission from [91].

4. Conclusions

Here, we elucidated the main features of chemical reactivity of SnSe$_2$. While the stoichiometric single crystal is chemically inert to ambient gases, the presence of selenium vacancies drastically affects surface chemical reactivity. The SnSe$_2-$x surface is transformed into SnO$_2$-skin-terminated SnSe$_2$, with a thickness of the SnO$_2$ skin estimated to be sub-nanometric.

Interestingly, while the self-assembled SnO$_2$/SnSe$_{2-x}$ heterostructure is an exceptional platform for detecting chemical species, as demonstrated for H$_2$, H$_2$O, NO$_2$, NH$_3$, and HS$_2$, the pristine SnSe$_2$ is unable to detect the same species. Thus, our results highlight the pivotal role of Se vacancies in metal dichalcogenides, which can transform the system from ambient-stable to an ultrasensitive gas sensor by tuning the stoichiometry.

Sensitivities of 0.43, 2.13, 0.11, and 1.06 [ppm]$^{-1}$ were reported for the detection of H$_2$, H$_2$S, NH$_3$, and NO$_2$, respectively. The corresponding limit of detection is 5 ppm, 10 ppb, 250 ppb, and 400 ppb for H$_2$, H$_2$S, NH$_3$, and NO$_2$, respectively.

Moreover, SnSe$_2$ is particularly suitable for THz photodetection, based on hot electrons. The response speed and the reactivity of the device are significantly improved thanks to the short channel, which exploits the localization of the electrostatic field and the high thermoelectric value of SnSe$_2$. Furthermore, the device has excellent stability, even when the uncapped active channel is exposed to air for long periods, thanks to the exceptional chemical inertness of the single stoichiometric SnSe$_2$ crystals. Accordingly, SnSe$_2$-based photodetectors represent suitable and promising candidates for imaging applications for homeland security and quality controls.

Author Contributions: Conceptualization, A.P., D.W.B., D.F., and G.D.; Methodology, C.-N.K., L.O., and C.S.L.; Investigation, D.W.B. and D.F.; Resources, D.F. and L.O.; Data curation, G.D. and D.F.; Writing—original draft preparation, G.D.; Writing—review and editing, G.D. and A.P.; Supervision, A.P. All authors have read and agreed to the published version of the manuscript.

Conflicts of Interest: The authors declare no conflict of interest.

References

1. Novoselov, K. Nobel Lecture: Graphene: Materials in the Flatland. *Rev. Mod. Phys.* **2011**, *83*, 837–849. [CrossRef]
2. Geim, A.K. Nobel Lecture: Random walk to graphene. *Rev. Mod. Phys.* **2011**, *83*, 851–862. [CrossRef]

3. Tao, Y.; Han, B.H.; Sui, Z.Y.; Tao, Y.; Han, B.H. Advanced porous graphene materials: From in-plane pore generation to energy storage applications. *J. Mater. Chem. A* **2020**, *8*, 6125–6143. [CrossRef]

4. Yang, L.; Yi, N.; Zhu, J.; Cheng, Z.; Yin, X.; Zhang, X.; Zhu, H.; Cheng, H. Novel gas sensing platform based on a stretchable laser-induced graphene pattern with self-heating capabilities. *J. Mater. Chem. A* **2020**, *8*, 6487–6500. [CrossRef]

5. Ahmadi, M.; Zabihi, O.; Jeon, S.; Yoonessi, M.; Dasari, A.; Ramakrishna, S.; Naebe, M. 2D transition metal dichalcogenide nanomaterials: Advances, opportunities, and challenges in multi-functional polymer nanocomposites. *J. Mater. Chem. A* **2020**, *8*, 845–883. [CrossRef]

6. Jalil, A.; Zhuo, Z.; Sun, Z.; Wu, F.; Wang, C.; Wu, X. A phosphorene-like InP_3 monolayer: Structure, stability, and catalytic properties toward the hydrogen evolution reaction. *J. Mater. Chem. A* **2020**, *8*, 1307–1314. [CrossRef]

7. Wu, J.; Liu, J.; Cui, J.; Yao, S.; Ihsan-Ul-Haq, M.; Mubarak, N.; Quattrocchi, E.; Ciucci, F.; Kim, J.-K. Dual-phase MoS2 as a high-performance sodium-ion battery anode. *J. Mater. Chem. A* **2020**, *8*, 2114–2122. [CrossRef]

8. Zeng, L.; Li, X.; Chen, S.; Wen, J.; Huang, W.; Chen, A. Unique hollow Ni-Fe@MoS$_2$ nanocubes with boosted electrocat-alytic activity for N2 reduction to NH_3. *J. Mater. Chem. A* **2020**, *8*, 7339–7349. [CrossRef]

9. Zu, G.; Guo, G.; Li, H.; Lu, Y.; Wang, R.; Hu, Y.; Wang, L.; Wang, J. Revealing the failure mechanism of transition-metal chalcogenides towards the copper current collector in secondary batteries. *J. Mater. Chem. A* **2020**, *8*, 6569–6575. [CrossRef]

10. Hu, G.; Fung, V.; Sang, X.; Unocic, R.R.; Ganesh, P. Superior electrocatalytic hydrogen evolution at engineered non-stoichiometric two-dimensional transition metal dichalcogenide edges. *J. Mater. Chem. A* **2019**, *7*, 18357–18364. [CrossRef]

11. Li, J.; Hong, W.; Jian, C.; Cai, Q.; He, X.; Liu, W. High-performance hydrogen evolution at a MoSe$_2$-Mo$_2$C seamless heterojunction enabled by efficient charge transfer. *J. Mater. Chem. A* **2020**, *8*, 6692–6698. [CrossRef]

12. Hu, H.; Shi, Z.; Khan, K.; Cao, R.; Liang, W.; Tareen, A.K.; Zhang, Y.; Huang, W.; Guo, Z.; Luo, X.; et al. Recent advances in doping engineering of black phosphorus. *J. Mater. Chem. A* **2020**, *8*, 5421–5441. [CrossRef]

13. Ozawa, A.; Yamamoto, M.; Tanabe, T.; Hosokawa, S.; Yoshida, T. Black phosphorus synthesized by solvothermal reaction from red phosphorus and its catalytic activity for water splitting. *J. Mater. Chem. A* **2020**, *8*, 7368–7376. [CrossRef]

14. Tian, Y.; Wang, H.; Li, H.; Guo, Z.; Tian, B.; Cui, Y.; Li, Z.; Li, G.; Zhang, H.; Wu, Y. Recent advances in black phosphorus/carbon hybrid composites: From improved stability to applications. *J. Mater. Chem. A* **2020**, *8*, 4647–4676. [CrossRef]

15. Ghosh, B.; Kumar, P.; Thakur, A.; Chauhan, Y.S.; Bhowmick, S.; Agarwal, A. Anisotropic plasmons, excitons, and electron energy loss spectroscopy of phosphorene. *Phys. Rev. B* **2017**, *96*, 035422. [CrossRef]

16. Sadhukhan, K.; Agarwal, A. Anisotropic plasmons, Friedel oscillations, and screening in 8-Pmmn borophene. *Phys. Rev. B* **2017**, *96*, 035410. [CrossRef]

17. Ottaviano, L.; Palleschi, S.; Perrozzi, F.; D'Olimpio, G.; Priante, F.; Donarelli, M.; Benassi, P.; Nardone, M.; Gonchigsuren, M.; Gombosuren, M.; et al. Mechanical exfoliation and layer number identification of MoS$_2$ revisited. *2D Mater.* **2017**, *4*, 045013. [CrossRef]

18. Yi, M.; Shen, Z. A review on mechanical exfoliation for the scalable production of graphene. *J. Mater. Chem. A* **2015**, *3*, 11700–11715. [CrossRef]

19. Gibaja, C.; Assebban, M.; Torres, I.; Fickert, M.; Sanchis-Gual, R.; Brotons-Alcázar, I.; Paz, W.; Palacios, J.J.; Michel, E.G.; Abellán, G.; et al. Liquid phase exfoliation of antimonene: Systematic optimization, characterization and electrocatalytic properties. *J. Mater. Chem. A* **2019**, *7*, 22475–22486. [CrossRef]

20. Adilbekova, B.; Lin, Y.; Yengel, E.; Faber, H.; Harrison, G.T.; Firdaus, Y.; El Labban, A.; Anjum, D.H.; Tung, V.; Anthopoulos, T.D. Liquid phase exfoliation of MoS$_2$ and WS$_2$ in aqueous ammonia and their application in highly efficient organic solar cells. *J. Mater. Chem. C* **2020**, *8*, 5259–5264. [CrossRef]

21. Hernandez, Y.; Nicolosi, V.; Lotya, M.; Blighe, F.M.; Sun, Z.; De, S.; McGovern, I.T.; Holland, B.; Byrne, M.; Gun'Ko, Y.K.; et al. High-yield production of graphene by liquid-phase exfoliation of graphite. *Nat. Nanotechnol.* **2008**, *3*, 563–568. [CrossRef] [PubMed]

22. Jin, Z.; Li, X.; Mullen, J.T.; Kim, K.W. Intrinsic transport properties of electrons and holes in monolayer transition-metal dichalcogenides. *Phys. Rev. B* **2014**, *90*, 045422. [CrossRef]

23. Edmonds, M.; Tadich, A.; Carvalho, A.; Ziletti, A.; O'Donnell, K.M.; Koenig, S.P.; Coker, D.F.; Özyilmaz, B.; Neto, A.H.C.; Fuhrer, M. Creating a Stable Oxide at the Surface of Black Phosphorus. *ACS Appl. Mater. Interfaces* **2015**, *7*, 14557–14562. [CrossRef] [PubMed]

24. Bergeron, A.; Ibrahim, J.; Leonelli, R.; Francoeur, S. Oxidation dynamics of ultrathin GaSe probed through Raman spectroscopy. *Appl. Phys. Lett.* **2017**, *110*, 241901. [CrossRef]

25. Shi, L.; Li, Q.; Ouyang, Y.; Wang, J. Effect of illumination and Se vacancies on fast oxidation of ultrathin gallium selenide. *Nanoscale* **2018**, *10*, 12180–12186. [CrossRef]

26. Lan, Y.; Chen, X.; Hu, C.; Cheng, Y.; Chen, Q. Penta-PdX2 (X = S, Se, Te) monolayers: Promising anisotropic thermoelectric materials. *J. Mater. Chem. A* **2019**, *7*, 11134–11142. [CrossRef]

27. Wu, D.; Jia, C.; Shi, F.; Zeng, L.; Lin, P.; Dong, L.; Shi, Z.; Tian, Y.; Li, X.; Jie, J. Mixed-dimensional PdSe$_2$/SiNWA hetero-structure based photovoltaic detectors for self-driven, broadband photodetection, infrared imaging and humidity sensing. *J. Mater. Chem. A* **2020**, *8*, 3632–3642. [CrossRef]

28. Yu, B.; Qi, F.; Zheng, B.; Hou, W.; Zhang, W.; Li, Y.; Chen, Y. Self-assembled pearl-bracelet-like CoSe$_2$-SnSe$_2$/CNT hollow architecture as highly efficient electrocatalysts for hydrogen evolution reaction. *J. Mater. Chem. A* **2018**, *6*, 1655–1662. [CrossRef]

29. Wei, Z.; Wang, L.; Zhuo, M.; Ni, W.; Wang, H.; Ma, J. Layered tin sulfide and selenide anode materials for Li- and Na-ion batteries. *J. Mater. Chem. A* **2018**, *6*, 12185–12214. [CrossRef]

30. Huang, Y.; Ling, C.; Liu, H.; Wang, S. Tuning electronic and magnetic properties of SnSe$_2$ armchair nanoribbons via edge hydrogenation. *J. Mater. Chem. C* **2014**, *2*, 10175–10183. [CrossRef]

31. Li, W.; Xiong, L.; Li, N.; Pang, S.; Xu, G.; Yi, C.; Wang, Z.; Gu, G.; Li, K.; Li, W.; et al. Tunable 3D light trapping architectures based on self-assembled SnSe$_2$ nanoplate arrays for ultrasensitive SERS detection. *J. Mater. Chem. C* **2019**, *7*, 10179–10186. [CrossRef]

32. Shafique, A.; Samad, A.; Shin, Y.-H. Ultra low lattice thermal conductivity and high carrier mobility of monolayer SnS2and SnSe$_2$: A first principles study. *Phys. Chem. Chem. Phys.* **2017**, *19*, 20677–20683. [CrossRef] [PubMed]

33. Shao, Z.; Fu, Z.-G.; Li, S.; Cao, Y.; Bian, Q.; Sun, H.; Zhang, Z.; Gedeon, H.; Zhang, X.; Liu, L.; et al. Strongly Compressed Few-Layered SnSe$_2$ Films Grown on a SrTiO$_3$ Substrate: The Coexistence of Charge Ordering and Enhanced Interfacial Superconductivity. *Nano Lett.* **2019**, *19*, 5304–5312. [CrossRef] [PubMed]

34. Zeng, J.; Liu, E.; Fu, Y.; Chen, Z.; Pan, C.; Wang, C.; Wang, M.; Wang, Y.; Xu, K.; Cai, S.; et al. Gate-Induced Interfacial Superconductivity in 1T-SnSe$_2$. *Nano Lett.* **2018**, *18*, 1410–1415. [CrossRef] [PubMed]

35. Kim, S.; Yao, Z.; Lim, J.-M.; Hersam, M.C.; Wolverton, C.; Dravid, V.P.; He, K. Lithium-Ion Batteries: Atomic-Scale Observation of Electrochemically Reversible Phase Transformations in SnSe$_2$ Single Crystals. *Adv. Mater.* **2018**, *30*, 1870393. [CrossRef]

36. Zhang, F.; Xia, C.; Zhu, J.; Ahmed, B.; Liang, H.; Velusamy, D.B.; Schwingenschlögl, U.; Alshareef, H.N. SnSe$_2$2D Anodes for Advanced Sodium Ion Batteries. *Adv. Energy Mater.* **2016**, *6*, 1601188. [CrossRef]

37. Zhou, X.; Zhou, N.; Li, C.; Song, H.; Zhang, Q.; Hu, X.; Gan, L.; Li, H.; Lü, J.; Luo, J.; et al. Vertical heterostructures based on SnSe$_2$/MoS$_2$ for high performance photodetectors. *2D Mater.* **2017**, *4*, 025048. [CrossRef]

38. Fan, Y.; Wang, J.; Zhao, M. Spontaneous full photocatalytic water splitting on 2D MoSe$_2$/SnSe$_2$ and WSe$_2$/SnSe$_2$ vdW heterostructures. *Nanoscale* **2019**, *11*, 14836–14843. [CrossRef]

39. Tan, P.; Chen, X.; Wu, L.; Shang, Y.Y.; Liu, W.; Pan, J.; Xiong, X. Hierarchical flower-like SnSe$_2$ supported Ag$_3$PO$_4$ nanoparticles: Towards visible light driven photocatalyst with enhanced performance. *Appl. Catal. B: Environ.* **2017**, *202*, 326–334. [CrossRef]

40. Wang, M.; Wang, Z.; Xu, X.; Duan, S.; Du, C. Tin diselenide-based saturable absorbers for eye-safe pulse lasers. *Nanotechnology* **2019**, *30*, 265703. [CrossRef]

41. Zhang, Y.; Liu, Y.; Lim, K.H.; Xing, C.; Li, M.; Zhang, T.; Tang, P.; Arbiol, J.; Llorca, J.; Ng, K.M.; et al. Tin Diselenide Molecular Precursor for Solution-Processable Thermoelectric Materials. *Angew. Chem. Int. Ed.* **2018**, *57*, 17063–17068. [CrossRef] [PubMed]

42. Luo, Y.; Zheng, Y.; Luo, Z.; Hao, S.; Du, C.; Liang, Q.; Li, Z.; Khor, K.A.; Hippalgaonkar, K.; Xu, J.; et al. n-Type SnSe$_2$ Oriented-Nanoplate-Based Pellets for High Thermoelectric Performance. *Adv. Energy Mater.* **2018**, *8*, 1702167. [CrossRef]

43. Lee, Y.K.; Luo, Z.-Z.; Cho, S.P.; Kanatzidis, M.G.; Chung, I. Surface Oxide Removal for Polycrystalline SnSe Reveals Near-Single-Crystal Thermoelectric Performance. *Joule* **2019**, *3*, 719–731. [CrossRef]

44. Lamuta, C.; Campi, D.; Pagnotta, L.; Dasadia, A.; Cupolillo, A.; Politano, A. Determination of the mechanical properties of SnSe, a novel layered semiconductor. *J. Phys. Chem. Solids* **2018**, *116*, 306–312. [CrossRef]

45. Yamashita, A.; Ogiso, O.; Matsumoto, R.; Tanaka, M.; Hara, H.; Tanaka, H.; Takeya, H.; Lee, C.-H.; Takano, Y. Influence of Oxidation in Starting Material Sn on Electric Transport Properties of SnSe Single Crystals. *J. Phys. Soc. Jpn.* **2018**, *87*, 065001. [CrossRef]

46. Chung, K.-M.; Wamwangi, D.M.; Woda, M.; Wuttig, M.; Bensch, W. Investigation of SnSe, SnSe$_2$, and Sn$_2$Se$_3$ alloys for phase change memory applications. *J. Appl. Phys.* **2008**, *103*, 083523. [CrossRef]

47. Guo, C.; Tian, Z.; Xiao, Y.; Mi, Q.; Xue, J. Field-effect transistors of high-mobility few-layer SnSe$_2$. *Appl. Phys. Lett.* **2016**, *109*, 203104. [CrossRef]

48. Palosz, B.; Salje, E. Lattice parameters and spontaneous strain in AX$_2$ polytypes: CdI$_2$, PbI$_2$ SnS$_2$ and SnSe$_2$. *J. Appl. Crystallogr.* **1989**, *22*, 622–623. [CrossRef]

49. Evans, B.L.; Hazelwood, R.A. Optical and electrical properties of SnSe$_2$. *J. Phys. D: Appl. Phys.* **1969**, *2*, 1507–1516. [CrossRef]

50. Mead, D.G.; Irwin, J.C. Raman spectra of SnS$_2$ and SnSe$_2$. *Solid State Commun.* **1976**, *20*, 885–887. [CrossRef]

51. Smith, A.J.; Meek, P.E.; Liang, W.Y. Raman scattering studies of SnS$_2$ and SnSe$_2$. *J. Phys. C Solid State Phys.* **1977**, *10*, 1321–1323. [CrossRef]

52. Taube, A.; Łapińska, A.; Judek, J.; Zdrojek, M. Temperature dependence of Raman shifts in layered ReSe$_2$ and SnSe$_2$ semiconductor nanosheets. *Appl. Phys. Lett.* **2015**, *107*, 013105. [CrossRef]

53. Henderson, M. The interaction of water with solid surfaces: Fundamental aspects revisited. *Surf. Sci. Rep.* **2002**, *46*, 1–308. [CrossRef]

54. Inamdar, A.N.; Som, N.N.; Pratap, A.; Jha, P.K. Hydrogen evolution and oxygen evolution reactions of pristine and alkali metal doped SnSe$_2$ monolayer. *Int. J. Hydrogen Energy* **2020**, *45*, 18657–18665. [CrossRef]

55. Deng, J.; Mo, Y.; Liu, J.; Guo, R.; Zhang, Y.; Xue, W.; Zhang, Y. In Vitro Study of SnS$_2$, BiOCl and SnS$_2$-Incorporated BiOCl Inorganic Nanoparticles Used as Doxorubicin Carrier. *J. Nanosci. Nanotechnol.* **2016**, *16*, 5740–5745. [CrossRef] [PubMed]

56. Cox, P.; Egdell, R.; Flavell, W.; Helbig, R. Observation of surface optical phonons on SnO$_2$ (110). *Vacuum* **1983**, *33*, 835–838. [CrossRef]

57. Nehasil, V.; Janeček, P.; Korotchenkov, G.; Matolin, V. Investigation of behaviour of Rh deposited onto polycrystalline SnO$_2$ by means of TPD, AES and EELS. *Surf. Sci.* **2003**, *532–535*, 415–419. [CrossRef]

58. Tanuma, S.; Powell, C.J.; Penn, D.R. Calculations of electron inelastic mean free paths (IMFPS). IV. Evaluation of calculated IMFPs and of the predictive IMFP formula TPP-2 for electron energies between 50 and 2000 eV. *Surf. Interface Anal.* **1993**, *20*, 77–89. [CrossRef]

59. Cox, D.F.; Hoflund, G.B. An electronic and structural interpretation of tin oxide ELS spectra. *Surf. Sci.* **1985**, *151*, 202–220. [CrossRef]

60. Wu, S.; Liu, C.; Wu, Z.; Miao, L.; Gao, J.; Hu, X.; Chen, J.; Zheng, Y.; Wang, X.; Shen, C.; et al. Realizing tremendous electrical transport properties of polycrystalline $SnSe_2$ by Cl-doped and anisotropy. *Ceram. Int.* **2019**, *45*, 82–89. [CrossRef]

61. Nagaraju, G.; Cha, S.M.; Sekhar, S.C.; Yu, J.S. Metallic Layered Polyester Fabric Enabled Nickel Selenide Nanostructures as Highly Conductive and Binderless Electrode with Superior Energy Storage Performance. *Adv. Energy Mater.* **2017**, *7*. [CrossRef]

62. Al-Hada, N.M.; Kamari, H.M.; Baqer, A.A.; Shaari, A.H.; Saion, E. Thermal Calcination-Based Production of SnO_2 Nanopowder: An Analysis of SnO_2 Nanoparticle Characteristics and Antibacterial Activities. *Nanomaterials* **2018**, *8*, 250. [CrossRef]

63. Zhang, W.; Li, M.; Xiao, X.; Huang, X.; Jiang, Y.; Fan, X.; Chen, L. In situ synthesis of ultrasmall SnO_2 quantum dots on nitrogen-doped reduced graphene oxide composite as high performance anode material for lithium-ion batteries. *J. Alloys Compd.* **2017**, *727*, 1–7. [CrossRef]

64. Bachvarova-Nedelcheva, A.; Iordanova, R.; Kostov, K.; Yordanov, S.; Ganev, V. Structure and properties of a non-traditional glass containing TeO_2, SeO_2 and MoO_3. *Opt. Mater.* **2012**, *34*, 1781–1787. [CrossRef]

65. Wakita, T.; Paris, E.; Kobayashi, K.; Terashima, K.; Hacisalihoğlu, M.Y.; Ueno, T.; Bondino, F.; Magnano, E.; Píš, I.; Olivi, L.; et al. The electronic structure of $Ag_1-xSn_1 + xSe_2$ (x = 0.0, 0.1, 0.2, 0.25 and 1.0). *Phys. Chem. Chem. Phys.* **2017**, *19*, 26672–26678. [CrossRef] [PubMed]

66. Cimino, A.; Gazzoli, D.; Valigi, M. XPS quantitative analysis and models of supported oxide catalysts. *J. Electron Spectrosc. Relat. Phenom.* **1999**, *104*, 1–29. [CrossRef]

67. Park, J.H.; Vishwanath, S.; Wolf, S.; Zhang, K.; Kwak, I.; Edmonds, M.; Breeden, M.; Liu, X.; Dobrowolska, M.; Furdyna, J.; et al. Selective Chemical Response of Transition Metal Dichalcogenides and Metal Dichalcogenides in Ambient Conditions. *ACS Appl. Mater. Interfaces* **2017**, *9*, 29255–29264. [CrossRef] [PubMed]

68. Paolucci, V.; D'Olimpio, G.; Kuo, C.-N.; Lue, C.S.; Boukhvalov, D.W.; Cantalini, C.; Politano, A. Self-Assembled $SnO_2/SnSe_2$ Heterostructures: A Suitable Platform for Ultrasensitive NO_2 and H_2 Sensing. *ACS Appl. Mater. Interfaces* **2020**, *12*, 34362–34369. [CrossRef]

69. Tian, K.; Wang, X.-X.; Yu, Z.-Y.; Li, H.-Y.; Guo, X. Hierarchical and Hollow Fe_2O_3 Nanoboxes Derived from Metal–Organic Frameworks with Excellent Sensitivity to H_2S. *ACS Appl. Mater. Interfaces* **2017**, *9*, 29669–29676. [CrossRef]

70. Wang, T.; Wang, Y.; Sun, Q.; Zheng, S.; Liu, L.; Li, J.; Hao, J. Boosted interfacial charge transfer in $SnO_2/SnSe_2$ hetero-structures: Toward ultrasensitive room-temperature H_2S detection. *Inorg. Chem. Front.* **2021**, *8*, 2068–2077. [CrossRef]

71. Zhang, D.; Wu, Z.; Zong, X. Flexible and highly sensitive H_2S gas sensor based on in-situ polymerized $SnO_2/rGO/PANI$ ternary nanocomposite with application in halitosis diagnosis. *Sens. Actuators B Chem.* **2019**, *289*, 32–41. [CrossRef]

72. Liu, L.; Wang, Y.; Dai, Y.; Li, G.; Wang, S.; Li, T.; Zhang, T.; Qin, S. In situ growth of $NiO@SnO_2$ hierarchical nanostructures for high performance H2S sensing. *ACS Appl. Mater. Interfaces* **2019**, *11*, 44829–44836. [CrossRef] [PubMed]

73. Gao, X.; Ouyang, Q.; Zhu, C.; Zhang, X.; Chen, Y. Porous MoO_3/SnO_2 Nanoflakes with n–n Junctions for Sensing H_2S. *ACS Appl. Nano Mater.* **2019**, *2*, 2418–2425. [CrossRef]

74. Eom, N.S.A.; Cho, H.-B.; Song, Y.; Go, G.M.; Lee, J.; Choa, Y.-H. Room-temperature H_2S gas sensing by selectively synthesized Cux(x=1, 2)O: SnO2 thin film nanocomposites with oblique & vertically assembled SnO_2 ceramic nanorods. *Sens. Actuators B Chem.* **2018**, *273*, 1054–1061.

75. Shen, Y.; Yamazaki, T.; Liu, Z.; Meng, D.; Kikuta, T.; Nakatani, N.; Saito, M.; Mori, M. Microstructure and H_2 gas sensing properties of undoped and Pd-doped SnO_2 nanowires. *Sens. Actuators B Chem.* **2009**, *135*, 524–529. [CrossRef]

76. Ghimbeu, C.M.; Lumbreras, M.; Siadat, M.; van Landschoot, R.C.; Schoonman, J. Electrostatic sprayed SnO_2 and Cu-doped SnO_2 films for H_2S detection. *Sens. Actuators B Chem.* **2008**, *133*, 694–698. [CrossRef]

77. Guo, X.; Ding, Y.; Liang, C.; Du, B.; Zhao, C.; Tan, Y.; Shi, Y.; Zhang, P.; Yang, X.; He, Y. Humidity-activated H_2S sensor based on $SnSe_2/WO_3$ composite for evaluating the spoilage of eggs at room temperature. *Sens. Actuators B Chem.* **2022**, *357*, 131424. [CrossRef]

78. Song, Z.; Wei, Z.; Wang, B.; Luo, Z.; Xu, S.; Zhang, W.; Yu, H.; Li, M.; Huang, Z.; Zang, J.; et al. Sensitive Room-Temperature H2S Gas Sensors Employing SnO_2 Quantum Wire/Reduced Graphene Oxide Nanocomposites. *Chem. Mater.* **2016**, *28*, 1205–1212. [CrossRef]

79. Moreira, L.C.; Cheng, W.-Y.; Fuh, H.-R.; Chien, W.-C.; Yan, W.; Fei, H.; Xu, H.; Zhang, D.; Chen, Y.; Zhao, Y.; et al. High Selectivity Gas Sensing and Charge Transfer of $SnSe_2$. *ACS Sens.* **2019**, *4*, 2546–2552. [CrossRef]

80. Pan, Q.; Li, T.; Zhang, D. Ammonia gas sensing properties and density functional theory investigation of coral-like $Au-SnSe_2$ Schottky junction. *Sens. Actuators B Chem.* **2021**, *332*, 129440. [CrossRef]

81. Rani, S.; Kumar, M.; Singh, Y.; Tomar, M.; Sharma, A.; Gupta, V.; Singh, V.N. NO2 Gas Sensor Based on $SnSe/SnSe_2$p-n Hetrojunction. *J. Nanosci. Nanotechnol.* **2021**, *21*, 4779–4785. [CrossRef] [PubMed]

82. Lee, L.; Chen, C.-W.; Manikandan, A.; Lee, S.-H.; Wang, Z.M.; Chueh, Y.-L. Phase-engineered $SnSe_x$ toward $SnSe_2/SnSe$ heterostructure with improved thermal conductance by a low-temperature plasma-assisted chemical vapor reaction. *Nano Energy* **2018**, *44*, 419–429. [CrossRef]

83. Liu, W.; Gu, D.; Li, X. AuPt Bimetal-Functionalized SnSe$_2$ Microflower-Based Sensors for Detecting Sub-ppm NO$_2$ at Low Temperatures. *ACS Appl. Mater. Interfaces* **2021**, *13*, 20336–20348. [CrossRef]

84. Wang, X.; Liu, Y.; Dai, J.; Chen, Q.; Huang, X.; Huang, W. Solution-Processed p-SnSe/n-SnSe$_2$ Hetero-Structure Layers for Ultrasensitive NO$_2$ Detection. *Chem. Eur. J.* **2020**, *26*, 3870–3876. [CrossRef]

85. Li, X.; Liu, W.; Huang, B.; Liu, H.; Li, X. Layered SnSe$_2$ microflakes and SnSe$_2$/SnO$_2$ heterojunctions for low-temperature chemiresistive-type gas sensing. *J. Mat. Chem. C* **2020**, *8*, 15804–15815. [CrossRef]

86. Song, J.C.W.; Rudner, M.S.; Marcus, C.M.; Levitov, L.S. Hot Carrier Transport and Photocurrent Response in Graphene. *Nano Lett.* **2011**, *11*, 4688–4692. [CrossRef]

87. Su, Y.; Ebrish, M.A.; Olson, E.J.; Koester, S.J. SnSe$_2$ field-effect transistors with high drive current. *Appl. Phys. Lett.* **2013**, *103*, 263104. [CrossRef]

88. Mics, Z.; Tielrooij, K.-J.; Parvez, K.; Jensen, S.A.; Ivanov, I.; Feng, X.; Müllen, K.; Bonn, M.; Turchinovich, D. Thermodynamic picture of ultrafast charge transport in graphene. *Nat. Commun.* **2015**, *6*, 7655. [CrossRef]

89. Bandurin, D.A.; Gayduchenko, I.; Cao, Y.; Moskotin, M.; Principi, A.; Grigorieva, I.V.; Goltsman, G.; Fedorov, G.; Svintsov, D. Dual origin of room temperature sub-terahertz photoresponse in graphene field effect transistors. *Appl. Phys. Lett.* **2018**, *112*, 141101. [CrossRef]

90. Viti, L.; Hu, J.; Coquillat, D.; Politano, A.; Knap, W.; Vitiello, M.S. Efficient Terahertz detection in black-phosphorus nano-transistors with selective and controllable plasma-wave, bolometric and thermoelectric response. *Sci. Rep.* **2016**, *6*, 20474. [CrossRef]

91. Guo, C.; Guo, W.; Xu, H.; Zhang, L.; Chen, G.; D'Olimpio, G.; Kuo, C.-N.; Lue, C.S.; Wang, L.; Politano, A.; et al. Ultra-sensitive Ambient-Stable SnSe$_2$-based Broadband Photodetectors for Room-Temperature IR/THz Energy conversion and Imaging. *2D Mater.* **2020**, *7*, 035026. [CrossRef]

92. Island, J.O.; Steele, G.A.; Van Der Zant, H.S.J.; Castellanos-Gomez, A. Environmental instability of few-layer black phosphorus. *2D Mater.* **2015**, *2*, 011002. [CrossRef]